Role of pairing correlations in the fission process

X. B. Wang [1,*] Yongjing Chen [2,†] G. X. Dong [1] Yang Su,[2] Zeyu Li [2] X. Z. Wu,[3] and Z. X. Li[3]

[1]*School of Science, Huzhou University, Huzhou 313000, China*
[2]*China Nuclear Data Center, China Institute of Atomic Energy, Beijing 102413, China*
[3]*Department of Nuclear Physics, China Institute of Atomic Energy, Beijing 102413, China*

The effects of the pairing force on the fission process including static and dynamics aspects are systematically studied, taking the induced fission of ^{240}Pu as an example. The Skyrme density functional theory (DFT) is adopted to calculate the static potential energy surface (PES), the nucleon localization function, etc. with the Hartree-Fock-Bogoliubov (HFB) and the HFB–Lipkin-Nogami (HFBLN) methods for the static part. The fission dynamics is studied based on the time-dependent generator coordinate method (TDGCM). The sensitivity of the calculation results to the pairing force is investigated by reducing and enhancing its strength from the normal one by 10%. Our results show that the pairing force plays a significant role in many aspects of the fission process. A very sensitive dependence of the mass tensor on the pairing strength is found, which has an obvious impact on the fission dynamics. The fission yields of ^{240}Pu with the normal pairing strength are consistent with the experimental data. However, the distribution of calculated fission yields becomes quite narrow for both enhanced and reduced pairing force cases, while the peak of the yields stays at the asymmetric fission side in the case of the reduced pairing strength, but in the case of enhanced pairing force it shifts toward the symmetric fission side. For the normal pairing force strength, our study shows that the calculated fission yield does not sensitively depend on the parameter related to the average particle number in the neck region for the determination of the scission line in the TDGCM approach within a reasonable range. It indicates that the fragments are formed early during the elongation of the fissioning nuclei, and a proper pairing force is essential for fission fragment distribution calculations.

I. INTRODUCTION

Nuclear fission, i.e., the phenomenon that one atomic nucleus separates into two or more fragments, was discovered more than 80 years ago [1,2]. The understanding of fission dynamics is important not only for its impact on basic science—e.g., the origin of the heavy elements in universe [3–5], the stability of superheavy nuclei [6], the more precise calculation of nuclear reactor antineutrinos [7], etc.—but also for applications, such as energy production, national security, nuclear waste disposal, etc. However, a fully microscopic description of nuclear fission is still lacking. Especially, the understanding of the fission mechanism based on the knowledge of nuclear forces and the quantum many-body theory remains elusive [8]. Currently, there are several approaches serving as microscopic tools for the prediction of nuclear fission observables, for example the time-dependent density functional theory (DFT) [9,10], which is still computationally expensive, and the time-dependent generator coordinate method (TDGCM) [11], which is based on the adiabatic approximation.

Most microscopic descriptions of nuclear fission, especially the theory within the adiabatic approximation, rely on the precise calculation of the potential energy surface (PES) in the collective space. From the calculation of the PES, it has been learned that the fission barrier heights, fission isomer excitation energies, and the collective inertia are sensitive to the strength of the pairing force [12–15]. The impact of the pairing correlations on static fission barriers has been investigated in Ref. [15], in which it was found that the height of the fission barriers can be lowered explicitly with the increase of the pairing force strength, and there is also a clear dependence of the fission barrier on the form of the pairing force. Within the method of the time-dependent superfluid local density approximation (TDSLDA), it has been shown that fission can be accelerated greatly by the increase of the pairing force [16]. In Ref. [14], the TDGCM calculation based on the covariant DFT was carried out for the fission of ^{226}Th, in which both the symmetric and asymmetric fission modes coexist. The asymmetric fission mode becomes more dominant with the reduction of the pairing force, while the symmetric fission mode is dominant with an enhanced pairing force. The experimental data can be reproduced by using a slightly increased pairing force in their calculation for ^{226}Th [14]. Recently, the effect of the dynamic pairing correlations on the fission process was studied in Refs. [17,18]. These studies showed that the pairing force can have a critical effect on the fission phenomena.

*xbwang@zjhu.edu.cn
†chenyj@ciae.ac.cn

However, it is still ambiguous how the pairing force affects the fission process. In most microscopic theories of fission dynamics, i.e., the TDGCM [11], the stochastic Langevin dynamics based on the DFT calculation [19], etc., the fission dynamics are mostly determined by the PES calculations in the collective space. Many aspects in the PES are influenced by the pairing force. Thus, it is still quite interesting to study how the pairing force influences the fission dynamics, which will be investigated systematically in this work within the framework of TDGCM.

The present paper will be developed as follows. We introduce the basic concepts in Sec. II. In Sec. III, we provide the calculation and analysis. Conclusions are drawn in Sec. IV.

II. THEORETICAL FRAMEWORK

A. The time-dependent Schrödinger-like equation

In this work, the fission of nuclei is approximated as a slow adiabatic process, and is driven by a few collective degrees of freedom. The time-dependent generator coordinate method (TDGCM) is used to describe this dynamic process. The detailed formalism can be found in Ref. [8]. Here, a brief introduction is given for a complete representation. In the GCM, the many-body state of the fissioning nuclei can be written in a general form as

$$|\Psi(t)\rangle = \int_q f(\mathbf{q}, t)|\Phi_\mathbf{q}\rangle d\mathbf{q}, \tag{1}$$

where the functions $\Phi_\mathbf{q}$ are known many-body functions parametrized by a set of collective variables $\mathbf{q}$. $f(\mathbf{q}, t)$ is the unknown weight function, which can be solved by inserting the above form into a time-dependent Schrödinger-like equation.

The exact solution is numerically expensive, and the Gaussian overlap approximation (GOA) is usually used. With GOA, the overlap between two generator states is given in a Gaussian form with dependence on the difference of collective variables $(\mathbf{q} - \mathbf{q}')$. Thus, in TDGCM-GOA, the equation to be solved has the form [8,20]

$$i\hbar \frac{\partial}{\partial t} g(\mathbf{q}, t) = \left[-\frac{\hbar^2}{2} \sum_{kl} \frac{\partial}{\partial \mathbf{q}_k} B_{kl}(\mathbf{q}) \frac{\partial}{\partial \mathbf{q}_l} + V(\mathbf{q}) \right] g(\mathbf{q}, t), \tag{2}$$

where $g(\mathbf{q}, t)$ is a complex wave function of the collective variables $\mathbf{q}$ and time t. It relates to the weight function $f(\mathbf{q}, t)$, and contains information on the dynamic system. $V(\mathbf{q})$ denotes the collective potential. The rank-2 tensor $B_{kl}(\mathbf{q})$ is the collective inertia, which is the inverse of the mass tensor, $\mathcal{M}^{-1}$. $V(\mathbf{q})$ and $\mathcal{M}^{-1}$ are obtained from static calculations, by using the Skyrme DFT in this work.

Fission fragment yields are the most important observables of fission, and can be derived from the function $g(\mathbf{q}, t)$. The continuity equation of the probability density $|g(\mathbf{q}, t)|^2$ is obtained by solving the equation

$$\frac{\partial}{\partial t} |g(\mathbf{q}, t)|^2 = -\nabla \cdot \mathbf{J}(\mathbf{q}, t), \tag{3}$$

where $\mathbf{J}(\mathbf{q}, t)$ is the probability current,

$$J(\mathbf{q}, t) = \frac{\hbar}{2i} B(\mathbf{q})[g^*(\mathbf{q}, t)\nabla g(\mathbf{q}, t) - g(\mathbf{q}, t)\nabla g^*(\mathbf{q}, t)]. \tag{4}$$

For the description of fission, one can divide the collective space into internal and external regions. In the internal region, the nucleus stays as a whole, while in the external region the nucleus becomes two fission fragments. The scission line, as a hypersurface, is determined artificially to distinguish these two regions. The flux of the probability current across the scission line, provides a measure of observing a pair of fission fragments at given time t. The integrated flux $F(\xi, t)$ for the surface element ξ on the scission hypersurface is calculated by

$$F(\xi, t) = \int_{t=0}^{t} dt \int_{\mathbf{q} \in \xi} \mathbf{J}(\mathbf{q}, t) \cdot d\mathbf{S}, \tag{5}$$

as in Ref. [20]. The yield of the fission fragment with mass number A can be calculated by

$$Y(A) = C \sum_{\xi \in \mathcal{A}} \lim_{t \to +\infty} F(\xi, t), \tag{6}$$

where $\mathcal{A}$ indicates a set of all surface elements ξ on the scission hypersurface with fragment mass A, and C is the normalization constant to make sure that the total yield is normalized to 200 as usual.

The TDGCM + GOA calculations are carried out by the software package FELIX (version 2.0) [21]. To gain the best numerical efficiency, the refined and adapted finite element meshes are used in the code FELIX, instead of the regular mesh adopted in the DFT calculation. To avoid the spurious reflection problem, the evolution collective variables are simulated in the symmetric space for the octupole deformation with the absorption boundary condition. The initial state of the collective Schrödinger-like equation (CSE) given in Eq. (2) is built as the superposition of collective eigenmodes in an extrapolated first potential well, similarly to Ref. [22]. The initial energy is chosen as 1 MeV above the first fission barrier. The weights of the mixing modes have a Gaussian shape as a function of the eigenenergies of the modes. The width of the Gaussian is fixed as 0.5 MeV. The dimension-10 Krylov space is used. The time step $\delta t = 2 \times 10^{-3}$ zs (1 zs = 10^{-21} s) is adopted in solving the evolution equation. The charge and mass yields are calculated after 20 zs. It has been tested that the resulted yields change little after this time.

B. The calculation of the static part

The Skyrme DFT is used to calculate the collective potential. We focus on the study of ^{240}Pu in this work, which is the popular choice of benchmark study. The calculation is done in (Q_{20}, Q_{30}) space spanning [0 b, 600 b] and [0 b$^{3/2}$, 60 b$^{3/2}$], with mesh steps of 2 b and 2 b$^{3/2}$, respectively. In this study, we use the SkM* [23] force, which is the popular choice in fission calculations [8,13,24]. In DFT, the pairing correlation is usually incorporated by the Hartree-Fock-Bogoliubov (HFB) method [25]. The Lipkin-Nogami (LN) method can be used as an approximated variation after projection method for

TABLE I. Convergence behavior as the function of the number of basis states N_{state} in the HFB calculation. The discrepancy between the HFB energy at the ground state by using different N_{state} and the value by using $N_{\text{state}} = 1100$ is listed. The other discrepancies, such as the HFB energy at large deformation point ($Q_{20} = 300$ b and $Q_{30} = 0$ b$^{3/2}$) and the inner fission barrier (B_I) and outer fission barrier (B_{II}) heights, are also listed. The units are MeV. The ratio of the mass tensor $\mathcal{M}_{22}$ (by the ATDHFB method) at the ground state by different N_{state} to the one by $N_{\text{state}} = 1100$ is given in the last column.

N_{state}	ΔE_{GS}	$\Delta E_{Q_{20}=300b}$	ΔB_I	ΔB_{II}	$\frac{\mathcal{M}_{22}(\text{GS})}{\mathcal{M}'_{22}(\text{GS})}$
800	0.533	2.288	0.171	0.558	1.063
1000	0.129	0.465	0.045	0.076	1.015
1200	−0.119	−0.394	−0.066	−0.028	0.984
1400	−0.312	−0.949	−0.062	−0.031	0.984
2000	−0.621	−1.457	−0.085	−0.097	0.978

the particle number restoration [26–29]. The surface-volume pairing force is used [30].

The code HFBTHO (V3.00) [31] is used in the calculations; therein the collective potential, mass tensor and neck properties, etc., can be provided. Detailed formulations can be found in Ref. [31]. The collective potential $V(\mathbf{q})$ is the result of energies from HFB or HFBLN calculation, plus a zero-point energy correction ϵ_{ZPE}. In this work, GCM and the adiabatic time-dependent HFB (ATDHFB) method are used for the calculations of the mass tensor. Thirty-one major shells of the axial harmonic-oscillator single-particle basis are used, and the full sets of them are further truncated into 1100 states. The truncation is mainly due to the memory limit and the growth of the computational cost by increasing the number of the basis state N_{state}. To specify the numerical errors caused by the basis truncation, we compare the HFB energies at several deformation points, the heights of inner and outer fission barriers, and the value of the mass tensor by using different N_{state}, as in Table I. In the table, the large value of $N_{\text{state}} = 2000$ is used for the test purpose. It is learned that restricting N_{state} to 1100 may lead to the error of HFB energy of roughly 1.5 MeV at large deformation. However, the errors of the fission barrier heights, which are calculated from the energy differences, are much smaller. The error of mass tensor due to the truncation of the basis is also small. Similar behavior is obtained by the HFBLN calculation. Following the prescription in Ref. [32], the basis deformation is varied with the required quadrupole deformation, $\beta = 0.05\sqrt{q_{20}}$, and the oscillator frequency is also changed with the quadrupole moment. In the current work, the density-dependent surface-volume pairing force is used, as given in Ref. [30]:

$$V(r_1, r_2) = V_0 \left[1 - \frac{1}{2}\frac{\rho}{\rho_0}\right]\delta(r_1 - r_2), \quad (7)$$

where V_0 is the pairing strength for the neutron or the proton, ρ is the total density, and $\rho_0 = 0.16$ fm^{-3}. The proton and neutron pairing strengths have been fitted to the empirical pairing gap of ^{240}Pu extracted from the three-point formula of the mass odd-even staggering. The cutoff of the pairing window 60 MeV is adopted. The proton and neutron pairing

TABLE II. The ground-state energy (with ZPE included) and barrier heights, extracted from the PES shown in Fig. 1. All units are MeV. B_I and B_{II} stand for the inner and outer barriers, relative to the ground state. The positions of the inner barrier in the PES for all these calculation are ($Q_{20} = 54$ b, $Q_{30} = 0$ b$^{3/2}$), and those of the outer barrier are listed in the table.

	E_{GS}	B_I	B_{II}	$\left(Q_{20}^{II}\text{ (b)}, Q_{30}^{II}\text{ (b}^{3/2})\right)$
HFB-90%	−1807.28	11.11	7.94	(120, 8)
HFB	−1808.89	9.30	7.05	(122, 8)
HFB-110%	−1812.60	7.25	5.83	(124, 8)
HFBLN	−1809.66	10.50	7.48	(122, 8)

strengths are taken to be −265.25 and −340.06 MeV in HFB calculations and −242.55 and −318.72 MeV in HFBLN, as the normal case, respectively.

To determine the scission contour, the neck operator is usually adopted in DFT [33] with the form of

$$\hat{Q}_N = \exp\left(-\frac{(z - z_N)^2}{a_N^2}\right), \quad (8)$$

where z denotes the main-axis coordinate, z_N is the neck position (its position is fixed at the lowest density position near the origin of the intrinsic frame [31]), and a_N is fixed to be 1.0 fm. The expectation value of the neck operator, $q_N = \langle\hat{Q}_N\rangle$ [see Eq. (8)], relates to the average particle number in the neck region. The determination of the scission contour is crucial in the calculation of the fission yields with the microscopic approach. Therefore, a small enough expected value of the neck operator is introduced and denoted as q_N^c. The region with q_N value larger than q_N^c is the prefission region, the one with q_N smaller than q_N^c is the postfission region, and the border between them is defined as the scission contour.

III. RESULTS AND DISCUSSION

A. The static part

In this work, we take the ^{239}Pu(n, f) reaction as an example to study the influence of the pairing force on the fission process. Both HFB and HFBLN are used in the calculations of PES, while various effects of the pairing force on the fission process are studied by comparison among the cases of normal, reduced, and enhanced pairing strength ($\pm 10\%$) within the HFB method.

1. Collective potential energy

The potential-energy surfaces of ^{240}Pu on the (Q_{20}, Q_{30}) plane calculated in four different cases are shown in Fig. 1. In general, the PESs and the minimum-energy fission paths from different calculations seem to be similar, as asymmetric fission is favored in all these calculations. The energies of the ground states and fission barriers are listed in Table II. The ground-state energies in HFBLN are lower than that in HFB due to the extra correlation energy from the LN method. The inner and outer barriers in HFB and HFBLN have similar relative energies compared to the ground state, and also have
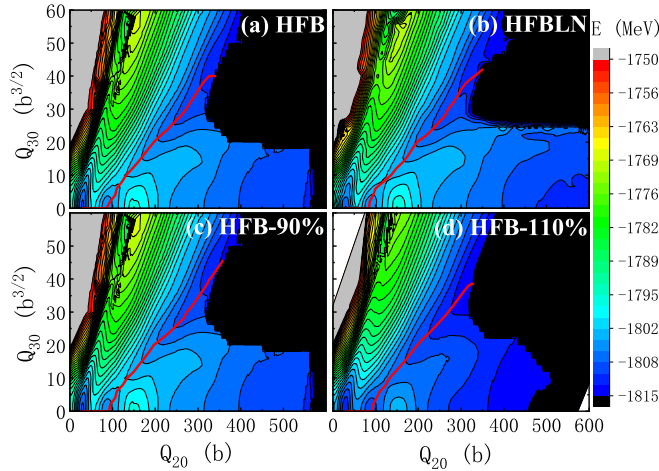
FIG. 1. Potential energy surfaces of ^{240}Pu with (a) HFB and (b) HFBLN approximation are shown. PESs in the HFB approximation with (c) 90% or (d) 110% of the HFB pairing strength are also shown, labeled by "HFB-90%" and "HFB-110%" respectively. The ZPE correction by GCM is included. The lowest-energy fission path is given as the red solid line.

FIG. 2. The Gaussian neck operator value q_N along the fission path is shown in panel (a). In panels (b) and (c), during the elongation along the fission path, the ratio of particle number of the heavy prefragment to the light one is given for charge and mass number, respectively. Results by using the HFB or HFBLN approximation are given. The values obtained from the 10% reduction or enhancement of the pairing strength within the HFB approximation are also listed.

the same quadrupole and octupole deformations. With the reduced (enhanced) pairing force, the ground state energy and also the fission barriers B_I and B_{II} become higher (lower).

2. Prefragments

During the elongation of the fissioning nucleus, the formations of the neck and prefragments are important for the estimation of fission products. After the determination of the neck position, one could estimate the mass and charge number for the light and heavy prefragments by integrating the one-body density. In Refs. [34–36], from the calculated density profiles or nucleon localization functions, it was learned that the prefragments could be formed quite early before reaching the scission point. In Fig. 2 we show the Gaussian neck operator value q_N (notice it is not q_N^c to define the scission line) and the ratio of the mass (charge) number of the heavy prefragment to the light one along the lowest-energy path. It is seen from the figure that the results obtained from HFBLN are between those obtained in cases with normal and enhanced pairing force by HFB methods but closer to the enhanced pairing force case. As shown in Fig. 2(a), in the large deformation region, the value of q_N decreases with the increase of Q_{20}, and finally drops to a very small value, indicating that the fragments are well separated. Such a drop will also cause an energy decrease of about 10 MeV. The discontinuity could be solved by adding more shape constraints in the collective space, as discussed in Ref. [37]. With the enhanced (reduced) pairing strength, the scission (taking $q_N^c = 4$) happens earlier (later) during the elongation, consistent with the results in Ref. [13]. In Figs. 2(b) and 2(c), it is shown that the ratios Z_H/Z_L and A_H/A_L drop from small Q_{20} until $Q_{20} \approx 230$ b, then keep stable until Q_{20} reaches about 280 barn. The prefragments may be formed at small deformation ($Q_{20} \approx 200$ b) already. Then, these ratios will slightly increase with Q_{20}, further increasing depending on the pairing strength. This effect

is more pronounced in the reduced pairing strength case, and finally the ratios Z_H/Z_L and A_H/A_L calculated in the reduced pairing strength case are larger than those in the enhanced and normal pairing strength cases. The reason for the slight increase of Z_H/Z_L and A_H/A_L is that the shell effect favor the heavy prefragment, which leads to the exchange of particles from light to heavy prefragments.

Moreover, as seen in Fig. 2, another pronounced feature that can be found is that a dramatic drop of q_N, Z_H/Z_L and A_H/A_L appears from prefission to postfission, which happens in the large Q_{20} region depending on the pairing force strength. The latter two indicate the dramatic change of the properties of two fragments from prefission to postfission. As is indicated by Bertsch *et al.* in Refs. [38,39] the pairing force plays an essential role in this process. The pairing jumps lead to the rearrangement of nucleons at the scission point, which eventually results in the dramatic change of properties of two fragments from prescission to postscission. It can be indirectly confirmed by the fact that the changes of Z_H/Z_L and A_H/A_L from prescission to postscission become much smaller in the reduced pairing force case compared with other cases.

The scission line is of essential importance for the calculation of fission properties. In Fig. 3, we show the scission lines obtained with $q_N^c = 4, 6, 8$, respectively. The fission fragments formed at the scission line are also shown in the figure. The scission line is the border between the pre- and postfission regions. In the first region the nucleus stays whole,
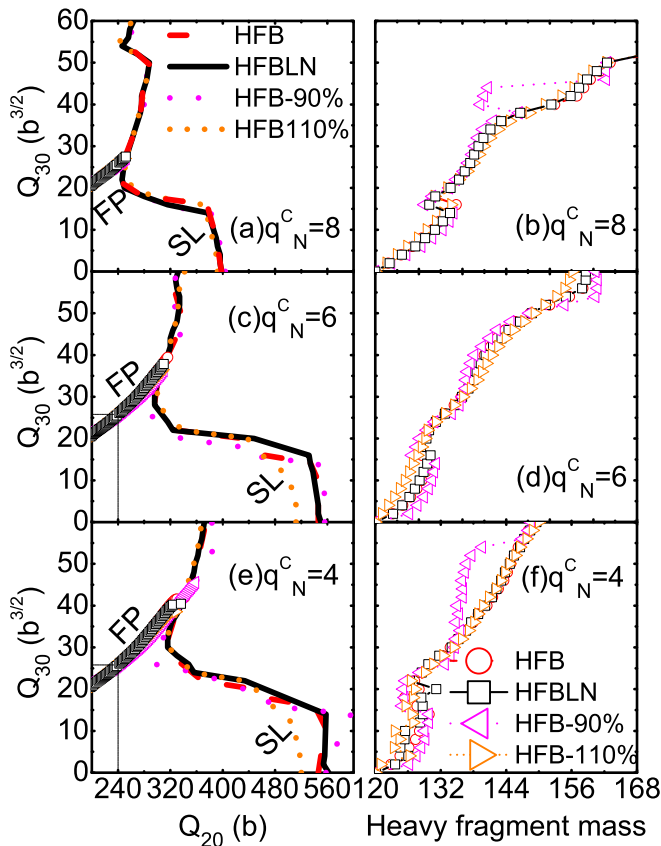
FIG. 3. The scission lines (labeled as "SL") using the criterion of average particle number in the neck region, $q_N^c = 8$, 6, and 4, are shown in panels (a), (c), and (e) respectively. In these panels, the lowest-energy fission path (labeled as "FP") is also given. The mass numbers of the heavy fragment formed at the scission lines determined by $q_N^c = 8$, 6, and 4 are given in panels (b), (d), and (f), respectively.

while in the later region it is assumed to be two separated fragments. From the density profiles, the nucleus becomes two well separated fragments when the value of q_N becomes close to zero. As seen from Fig. 2(a), for the HFB and HFBLN calculations with the normal pairing strength, q_N as a function of Q_{20} around $q_N = 6$ or 8 is still continuous and smooth, and q_N becomes very small after $q_N = 4$. Thus, $q_N^c = 4$ might be a proper choice for the scission line in following calculations. However, for the enhanced pairing force strength, q_N decreases very quickly after $q_N = 6$ or larger value, while, for the reduced force strength, it happens at around $q_N = 4$ or smaller value. It implies that the proper choice of the q_N^c value for determining the scission contour may depend on the pairing force strength.

In Figs. 3(a), 3(c), and 3(e), the patterns of the scission lines from different treatments of the pairing correlations or different pairing strengths are quite similar. For ^{240}Pu, symmetric fission happens at large quadrupole deformation ($Q_{20} > 500$ b for the q_N^c taken to be 4 and 6, and $Q_{20} \approx 400$ b for $q_N^c = 8$). The shortest elongation in the scission line appears at ($Q_{20} \approx 240$–320 b, $Q_{30} \approx 25$–30 b$^{3/2}$), corresponding to the heavy fragment close to ^{132}Sn. Then the scission line

turns toward the upper-right direction at very large asymmetry. The comparison among the calculation results with different pairing force strengths indicates that, with the increase of the pairing strength, the prescission domain shrinks, especially for the region close to symmetric fission, and the corresponding scission line becomes smoother. The crossing point of the fission path and the scission line is around $Q_{30} \approx 40$ b$^{3/2}$ for $q_N^c = 4$ or 6. The corresponding crossing point is at $Q_{30} \approx 30$ b$^{3/2}$ for $q_N^c = 8$. For the $q_N^c = 8$ case, it is seen in the figure that the prefission region becomes explicitly smaller and the discrepancies between different treatments of pairing correlation or pairing strength become quite small.

Now let us look at the right panels, i.e., Figs. 3(b), 3(d), and 3(f), which show the mass number of the heavy fission fragment A_H formed at the scission point against the octupole moment Q_{30}. In the region of Q_{30} smaller than 20 b$^{3/2}$, with the decrease of the pairing strength, the asymmetry between heavy and light fragments increases. In the region of about $20 < Q_{30} < 30$ b$^{3/2}$, the scission line bends from the largest elongation to the shortest elongation, and all the calculations present nearly similar mass asymmetry of fragments. Then, in the larger Q_{30} region, the asymmetry between heavy and light fragments is smaller for the reduced pairing force strength case compared with other cases, which may lead to a narrower mass distribution. The discrepancies between HFB and HFBLN calculations are quite small. And one important feature can be seen from these panels is that for the scission line with larger q_N^c the fission fragment distribution is more spread out, and at the same octupole moment it corresponds to a larger asymmetry of the fission fragments. To illustrate the formation of prefragments in fissioning nuclei, we plot the nucleon localization function (NLF) along the fission path in Fig. 4. It shown in Refs. [40–42] that the NLF is more efficient than the matter density distribution to quantify the clustering phenomena. The concentric rings in the figure indicate the enhanced localization of nucleons, which relates to the shell structure. The ring structure is more distinct for the proton NLF, as the occupied shell orbitals of the proton are less than those of the neutron, within the similar volume [42]. The ground state of ^{240}Pu has the quadrupole moment of 30 barn, and $Q_{20} = 86$ b in its isomeric state. One heavy fragment with spherical shape and one light fragment with prolately deformed shape start to form already at the quadrupole moment of 200 b. During the elongation, in the case of enhanced pairing, the ring structures in the light and heavy fragments are nearly closed at $Q_{20} = 328$ b. At $Q_{20} = 350$ b, the concentric rings become closed in two separated fragments for all three cases of enhanced, normal, and reduced pairing strength, and the two fragments are well separated for the enhanced pairing force. Interestingly, the figure shows that the pairing force plays a key role in the neck formation and rupture and the stronger pairing force leads to an earlier separation of fragments from the comparison of NLFs obtained in three cases of different pairing force strengths.

3. Mass tensor

The mass tensor is involved in the kinetic energy term in Eq. (2), and reflects the response of the fissioning system to
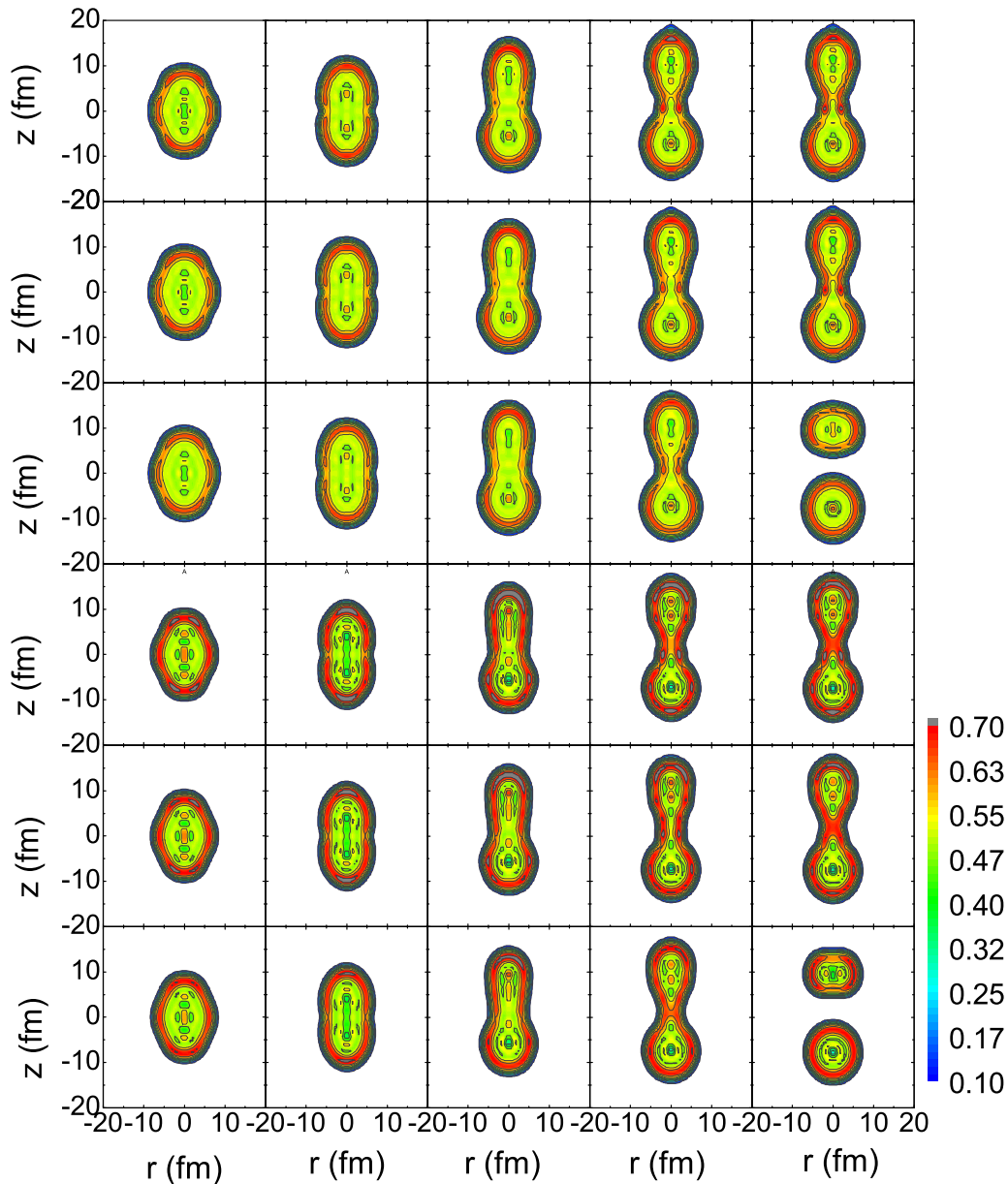
FIG. 4. The top three rows are for the neutron NLF. The first, second, and third rows are calculated with the reduced (90%), original, and enhanced (110%) pairing strength, in the HFB approximation. The three rows at the bottom are the proton NLF. The fourth, fifth and sixth are from the cases of reduced, original, and enhanced pairing force, respectively. From left to right columns, NLFs with different deformations along the lowest-energy fission path are given, for the quadrupole moments of 30, 86, 200, 328, and 350 b, respectively.

the collective coordinate changes, i.e., the change of Q_{20} and Q_{30} in this work. The mass tensor is inversely proportional to the probability current and thus is one of the important ingredients for the calculation of fission yields as given in Eqs. (4)–(6). In the current work, the perturbative cranking approximation is used for the calculation of the mass tensor. The elements of the mass tensor $\mathcal{M}_{22}$, $\mathcal{M}_{33}$, and $\mathcal{M}_{23}$ as function of Q_{20} along the lowest-energy fission path are shown in Fig. 5. The mass tensor given by ATDHFB is larger than that by GCM. As explained in Ref. [8], it is caused by the missing correlations in the GCM method. With the increase of the

elongation deformation, the $\mathcal{M}_{22}$ and $\mathcal{M}_{33}$ gradually decrease and are saturated at large Q_{20}, and the $\mathcal{M}_{23}$ becomes negative with large fluctuation except in the case of enhanced pairing force for which the $\mathcal{M}_{23}$ is rather stable with respect to the change of Q_{20}. The trend in HFB is similar to that in HFBLN. Moreover, the mass tensor is rather sensitive to the pairing strength. As seen in Fig. 5, M_{22} and the absolute value of M_{23} increase with the the decrease of pairing force. For the reduced pairing force case, the fluctuations of M_{22} and M_{23} become very large, while M_{33} is not so pronounced with the change of pairing force except at very small elongation deformation.
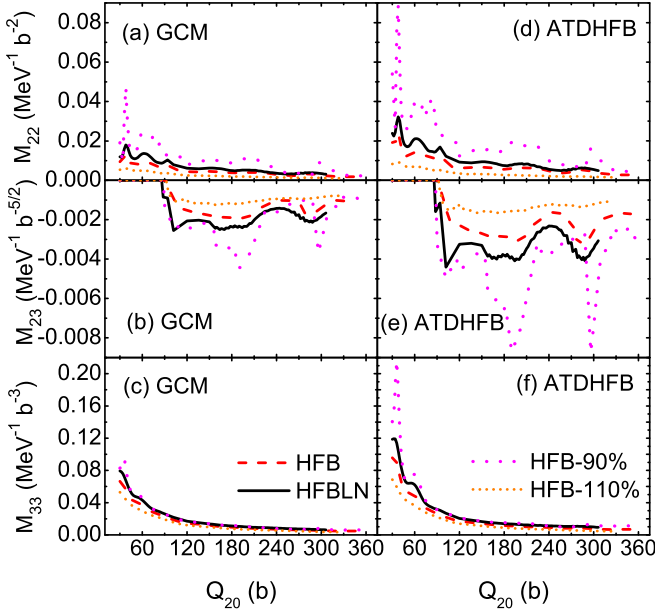
FIG. 5. $\mathcal{M}_{22}$ (top panel), $\mathcal{M}_{23}$ (middle panel), and $\mathcal{M}_{33}$ (bottom panel) of the mass tensor are shown for the quadrupole moment along the static fission path. The left column is from using the GCM method, and the right column is derived by ATDHFB method.

B. The dynamic part

In this part we will show the calculation results of mass and charge distributions of fragments based on the TDGCM-GOA framework. We will first show the calculation results with the normal pairing force strength, with comparison to the experimental data. Then, the sensitivity of pairing correlation to the yields of fragments will be studied using the reduced and enhanced pairing forces.

1. Fission yields calculated with the normal pairing strength

The calculation results based on the TDGCM-GOA framework are shown in Fig. 6. $q_N^c = 4$ is used as the determination of the scission line in this calculation. The figure indicates that the calculated mass and charge yields by using the collective potential energy surfaces with the HFB and HFBLN methods are similar, and the discrepancies between results by using mass tensors from GCM and from ATDHFB methods are small. As the mass resolution in the experiments is much larger than one mass unit, the data points in the figure from Refs. [43–45] are obtained after the treatment of convolution. As suggested by Refs. [20,22] and others, for a better comparison with the experimental data, a smoothing function with a Gaussian form is often used after the evolution of the TDGCM. The width of the Gaussian function is chosen as 4.0 for the mass yield and 1.6 for the charge yield, as suggested by Ref. [20]. The raw yields before the convolution are also shown in the figure. Without the convolution, the maximum of the yields matches the experimental data, but the distribution of the yields is narrower. After the smoothing process done by the convolution, the position of the peak is kept the same, and the height becomes lower than the peak of the raw yields by
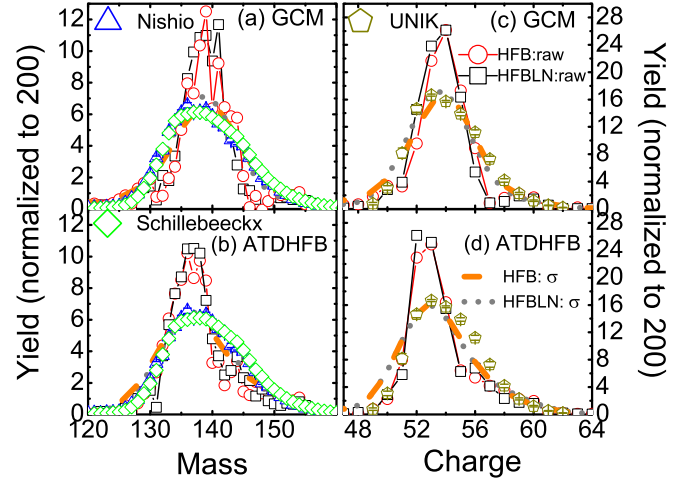
FIG. 6. Calculated preneutron mass yields [panels (a) and (b)] and charge yields [panels (c) and (d) are compared with the data. Only the heavy fragments are represented. The results using the input from HFB or HFBLN calculation are labeled as "HFB" or "HFBLN", respectively. The raw yields from TDGCM are shown with the label "raw". The convoluted results by a Gaussian smoothing function with $\sigma = 4$ (mass yield) or 1.6 (charge yield) are shown with the label "σ". In panels (a) and (c) the mass tensor from the GCM method is used, and in panels (b) and (d) the mass tensor from the ATDHFB method is used. The data for preneutron mass yield are from Refs. [43,44], and the charge yield data are from Ref. [45].

roughly 40%. The width of the convoluted yield distribution becomes larger and is close to the data.

2. The effect of the pairing correlations

To test the influence of the pairing correlations on the fission dynamics, we calculate the fission yields based on the PES, mass tensor, etc. obtained by HFB method with normal, reduced and enhanced pairing force, respectively. The results are shown in Fig. 7. The choice of $q_N^c = 4$ as the scission
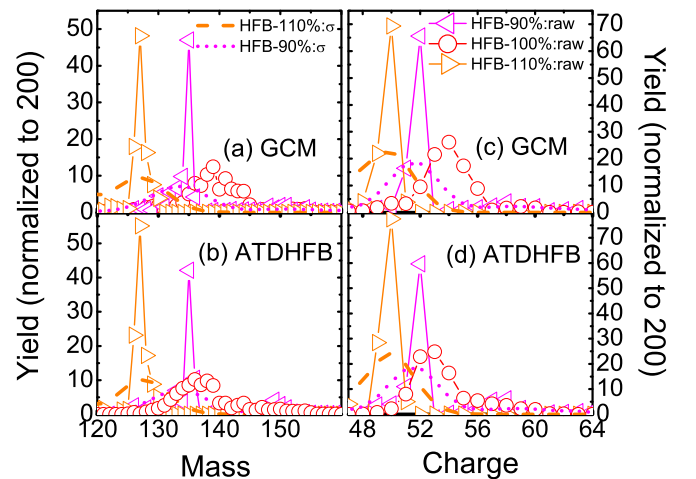
FIG. 7. The same as Fig. 6, but for the yields calculated by the inputs from the different strengths of the pairing force in the HFB approximation.

TABLE III. The peak of the yields from the TDGCM calculation, and the fragments indicated at the end of the lowest-energy fission path (determined by $q_N = 4$ scission line as shown in Fig. 3) in the static PES (labeled as "PES"). The particle number of the fragment given by PES is kept as the integer nearest to its value, thus it has "±1" uncertainty. The label "GCM" or "ATDHFB" denotes that the TDGCM calculation (using the $q_N = 4$ scission line) is done by using the mass tensor from the GCM or ATDHFB method. Only the heavy fragments are listed. The charge number of the heavy peak in the experimental data is 53 [45]. The preneutron mass number of the heavy peak from experiments is 136 [43] or 137 [44].

	HFBLN	HFB	HFB-90%	HFB-110%
$(Z_H, A_H)_{PES}$	(54,140)	(54,140)	(52,136)	(54,139)
$(Z_H, A_H)_{GCM}$	(54,141)	(54,139)	(52,135)	(50,127)
$(Z_H, A_H)_{ATDHFB}$	(53,136)	(53,136)	(52,135)	(50,127)

line is used. It is seen from the figure that, within the 10% variations of the pairing strength, the calculated yields have changed a lot, indicating the essential role of the pairing correlations on the fission dynamics. We find that the yields at the peak of fragment mass (charge) distributions calculated with the reduce or enhanced pairing strength are too high and the off-peak yields are too suppressed. The peak by the enhanced pairing force moves toward the direction of the symmetric fission. The peak using the reduced pairing force with GCM or ATDHFB mass tensor stays near the experimental peak (mass ≈136–137 [43,44], and charge ≈53 [45]). The large effect of varying the pairing strength on the yield calculation was also found in Ref. [14]. In Ref. [18], it is learned that with the dynamic pairing correlation the calculated fission yields have a distribution similar to those from enhancing pairing force strength by 10%.

We collect the peak position of the charge and mass yields from different calculations in this work in Table III for the comparison. The most probable yields for four cases obtained by the lowest-energy fission path in the PES are also listed, and have similar values close to the experimental data. The peak of the yields by the PES from HFB calculations is nearly the same as from the HFBLN calculation. For the results from dynamic calculations, the maximum yield by using the mass tensor from the GCM method stays close to that from the static fission path, but with the ATDHFB mass tensor it moves by several units toward the direction of the symmetric mode. From Table III, the peak given by the reduced pairing force is still close to the experimental data. However, the mass (charge) at the peak region with the enhanced pairing force becomes close to the symmetric mode. It seems that the flux flows mostly through the path with the smaller octupole deformation, which deviates from the lowest-energy fission path.

In the previous subsection, as shown in Fig. 2, it was seen that the choice of q_N^c for the determination of scission contour seems to depend on the pairing force strength. In Fig. 3, with larger q_N^c value, the prescission domain will shrink and the fragments formed at the scission line could have a broader distribution, and vice versa. For the larger q_N^c case, the discrepancies of the scission contour and the distributions
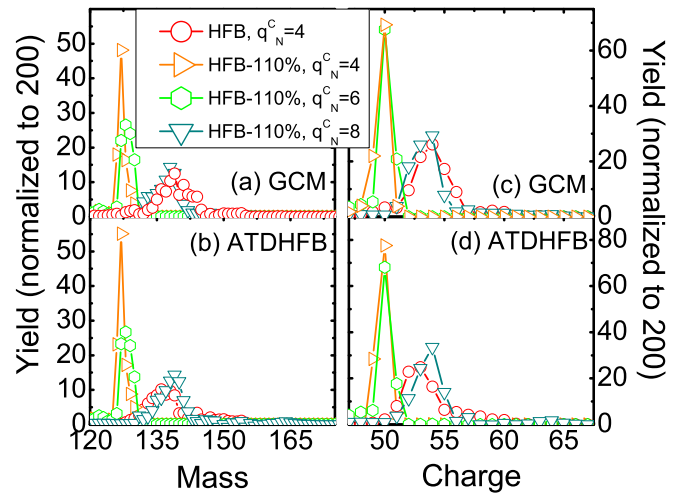
FIG. 8. The fission yields calculated by using the scission lines determined by different q_N criteria, with the inputs of the enhanced pairing force. Left and right panels are for the mass and charge yields, respectively. In panels (a) and (c) the calculations are done using the GCM mass tensor, and in panels (b) and (d) the calculations are performed with the ATDHFB mass tensor. Only the raw yields from TDGCM are shown. The results of the normal pairing strength with HFB approximation are also given for comparison.

of the fission fragments between different pairing treatments or pairing strengths are smaller.

To study its influence on the dynamic calculations, we perform the TDGCM calculations by varying the q_N^c values, for the enhanced and reduced pairing force, and the results are shown in Figs. 8 and 9, respectively. In Fig. 8, for the case of the enhanced pairing strength, the distribution of the yields using the $q_N^c = 6$ scission line is similar to the distribution from using the $q_N^c = 4$ scission line. The peak of the fission yield stays the same, tending toward the symmetric fission channel. As seen in Fig. 2, in the smaller deformation region, with Q_{20} moment roughly about 200–300 b, the mass and charge
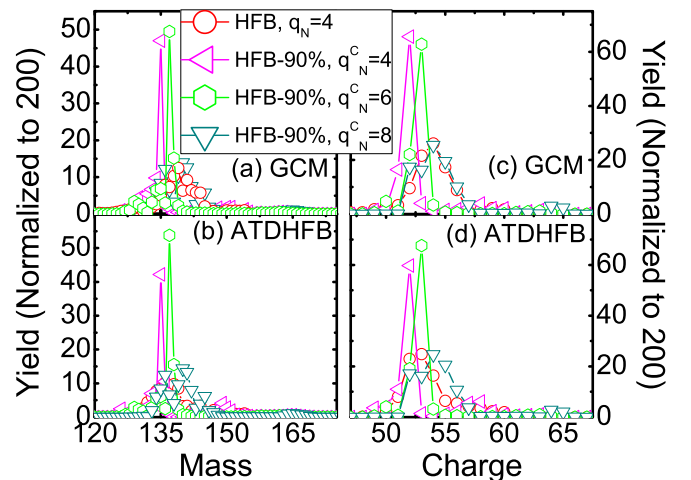
FIG. 9. The same as Fig. 8, but for the case of the reduced pairing strength.

number of the prefragments are stable during the elongation, until the sudden drop of the neck size q_N, after which the two fragments are well separated and the asymmetry between the two fragments becomes small. For the enhanced pairing force, the drop of the neck size happens around larger q_N values and at smaller deformation. Thus, if the postfission region is included in the dynamic calculation improperly as the "prefission" region, the yield distribution will tend toward the symmetric fission channel. With $q_N^c = 4$, the same choice as the normal pairing strength, the prefission region is too large for the case of the enhanced pairing force. For q_N value larger than 8, nice continuity is satisfied for most deformation points. Using the scission line determined by $q_N^c = 8$, the peak turns toward the asymmetric fission channel, reproducing the experimental data. And, its width also becomes close to the dynamic calculation results from the HFB approximation with the normal pairing force and $q_N^c = 4$ scission line.

In Fig. 9, for the case of the reduced pairing force, by comparing the two cases of $q_N^c = 4$ and $q_N^c = 6$, the peak of the yield distribution for the latter case moves toward the right, the direction of the more asymmetric fission mode (from 135 to 137 for the mass number, and from 52 to 53 for the charge number), which is closer to the experimental data. But the width of the yield distribution is still quite narrow. Using the $q_N^c = 8$ scission line, the width of the fission yield distribution becomes larger and its peak stays similar to the $q_N^c = 6$ one. For $q_N^c = 4$ and 6 scission lines in Fig. 3, it can be seen that for the case of the reduced pairing force the distribution of the fission fragments formed at the scission line is explicitly narrower compared to that by using the normal or enhanced pairing force strength, especially at the region around the crossing point of scission line and fission path. For the $q_N^c = 8$ case, the fission fragments on the scission line have a wider distribution.

In Fig. 10, we show the dynamic calculation results of changing q_N^c, for the HFB and HFBLN methods with the normal pairing strength. It is seen, that varying q_N^c from 4 to 8, the calculation results of the fission yields with the normal pairing strength are similar, except for the extra tiny peak appearing at the very asymmetric fission channel by using the $q_N^c = 8$ scission line. Thus $q_N^c = 8$ may not be a proper choice of scission contour. The discrepancies between HFB and HFBLN methods are small, which is consistent with the results shown in Fig. 3 where the scission lines and the fission fragments obtained by using these two methods are quite similar. With the increase of q_N^c for the scission contour, the prefission domain shrinks explicitly and the fission fragments formed at the scission contour have a wider distribution, which is responsible for the extra small peak in the asymmetric fission channel. However, around the crossing point of the fission path and scission contour, the mass and charge particle numbers of the fission fragments are similar. At around $q_N = 8$, the deformation is much smaller than the configurations around the $q_N = 4$. The energy curve is very smooth, and q_N and other quantities are continuous with the neighboring deformations. It can be regarded as proof that the fission fragments are already formed at small deformation states and are quite stable during the elongation process, which can also be seen clearly in Figs. 2(b), 2(c), and 4.
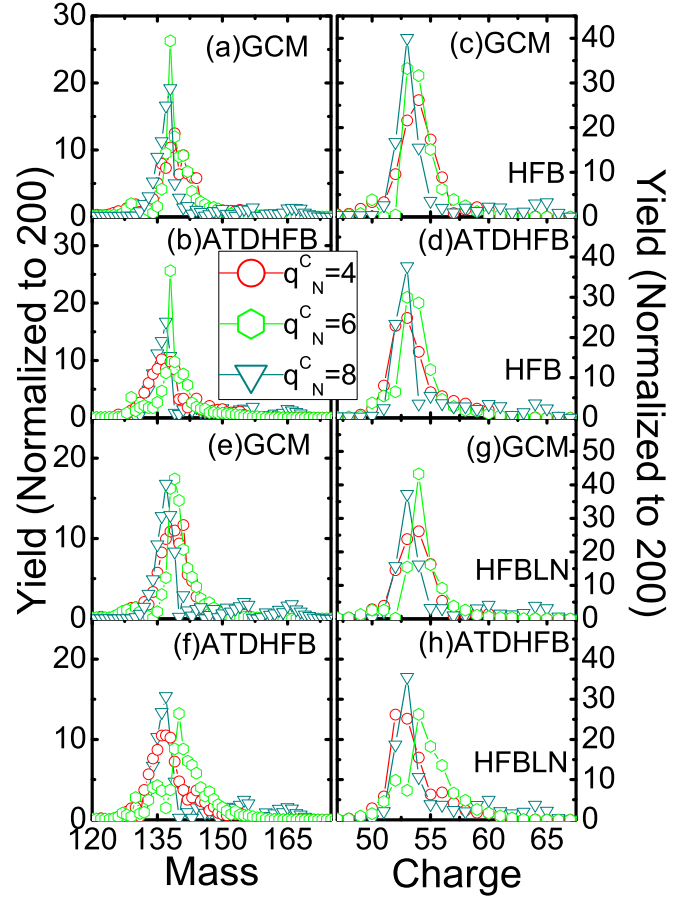
FIG. 10. The same as Figs. 8 and 9, but for the yields calculated by using HFB [panels (a)–(d)] and HFBLN [panels (e)–(h)] approximations.

IV. SUMMARY AND CONCLUSION

In present work, we have mainly studied the role of the pairing force in the fission process, taking the example of the ^{239}Pu(n, f) reaction. The HFB and HFBLN methods with SkM*-DFT are used. To test the sensitivity of the calculation results to the strength of the pairing correlation, we reduce or enhance the pairing force in the HFB by 10%. The static PESs by using HFB and HFBLN are very similar. The increase of the pairing force strength leads to a lower ground-state and isomeric-state energies and fission barrier. Simultaneously, the collective mass tensor becomes smaller and has less fluctuation against deformation. Moreover, with the reduction of the pairing force strength, the nucleus requires larger deformation to reach scission. In this case, due to the competition between the pairing force and shell effect, the fragments formed at the scission line have a narrower distribution close to the minimized-energy fission path in the PES, which is mainly driven by the shell effect. The formation of the prefragments is also influenced by the pairing force as in the case of enhanced pairing; the prefission domain shrinks and the scission line is smoother for the same q_N^c. The increase of q_N^c also leads to the shrinking of the prescission domain, in which the elongation of nucleus is smaller and the difference among

the distributions of fission fragments obtained with different pairing strengths become smaller.

The dynamic calculations are performed within the TDGCM-GOA framework and the yields obtained by using the PES calculated with HFB and HFBLN are similar and close to experimental data. Concerning the effect of pairing force on the fission dynamics, we vary the pairing force strength by 10%, and it is observed that the widths of the yield distributions for both enhanced and reduced pairing force become quite narrow. The peak position of the distribution is closer to the symmetric fission channel for the enhanced pairing strength case, and does not change much for the reduced pairing force case. Concerning the influence of the different q_N^c on the results, we find that the increase of q_N^c perhaps could improve the yield calculations for the enhanced or reduced pairing force cases. For the enhanced pairing force, the sudden drop of the neck size occurs at larger q_N and smaller deformation. If one chooses the same value of q_N^c as in the normal pairing force strength case, the configurations in the postfission region might be incorporated improperly,

thus a larger q_N^c is needed for a reasonable calculation. For the case of reduced pairing force strength, the distribution of fission fragments at the scission contour would become wider with the increase of q_N^c, especially around the end of the fission path. Thus, after the increase of q_N^c, one can obtain a wider distribution of the fission yields. However, for the normal pairing force strength, the calculation results are rather robust against the variation of q_N^c, even for the $q_N^c = 8$ case. It indicates that the fission fragments are already formed at small deformations and a proper pairing force is of essential importance to get a reasonable dynamic calculation.

[1] L. Meitner and O. R. Frisch, Nature (London) **143**, 239 (1939).

[2] O. Hahn and F. Strassmann, Naturwissenschaften **27**, 11 (1939).

[3] G. Martínez-Pinedo, D. Mocelj, N. Zinner, A. Kelić, K. Langanke, I. Panov, B. Pfeiffer, T. Rauscher, K.-H. Schmidt, and F.-K. Thielemann, Prog. Part. Nucl. Phys. **59**, 199 (2007).

[4] S. Goriely, J.-L. Sida, J.-F. Lemaître, S. Panebianco, N. Dubray, S. Hilaire, A. Bauswein, and H.-T. Janka, Phys. Rev. Lett. **111**, 242502 (2013).

[5] S. A. Giuliani, G. Martínez-Pinedo, and L. M. Robledo, Phys. Rev. C **97**, 034323 (2018).

[6] Y. T. Oganessian and V. K. Utyonkov, Rep. Prog. Phys. **78**, 036301 (2015).

[7] A. C. Hayes, G. Jungman, E. A. McCutchan, A. A. Sonzogni, G. T. Garvey, and X. B. Wang, Phys. Rev. Lett. **120**, 022503 (2018).

[8] N. Schunck and L. M. Robledo, Rep. Prog. Phys. **79**, 116301 (2016).

[9] T. Nakatsukasa, S. Ebata, P. Avogadro, L. Guo, T. Inakura, and K. Yoshida, J. Phys.: Conf. Ser. **387**, 012015 (2012).

[10] A. Bulgac and M. M. Forbes, Phys. Rev. C **87**, 051301(R) (2013).

[11] J. F. Berger, M. Girod, and D. Gogny, Comput. Phys. Commun. **63**, 365 (1991).

[12] S. A. Giuliani and L. M. Robledo, Phys. Rev. C **88**, 054325 (2013).

[13] N. Schunck, D. Duke, H. Carr, and A. Knoll, Phys. Rev. C **90**, 054305 (2014).

[14] H. Tao, and J. Zhao, and Z. P. Li, T. Nikšić, and D. Vretenar, Phys. Rev. C **96**, 024319 (2017).

[15] S. Karatzikos, A. V. Afanasjev, G. A. Lalazissis, and P. Ring, Phys. Lett. B **689**, 72 (2010).

[16] A. Bulgac, S. Jin, K. J. Roche, N. Schunck, and I. Stetcu, Phys. Rev. C **100**, 034615 (2019).

[17] Y. Qiang, J. C. Pei, and P. D. Stevenson, Phys. Rev. C **103**, L031304 (2021).

[18] J. Zhao, T. Nikšić, and D. Vretenar, Phys. Rev. C **104**, 044612 (2021).

[19] J. Sadhukhan, W. Nazarewicz, and N. Schunck, Phys. Rev. C **93**, 011304(R) (2016)

[20] D. Regnier, N. Dubray, N. Schunck, and M. Verrière, Phys. Rev. C **93**, 054611 (2016).

[21] D. Regnier, N. Dubray, M. Verriere, and N. Schunck, Comput. Phys. Commun. **225**, 180 (2018).

[22] D. Regnier, N. Dubray, and N. Schunck, Phys. Rev. C **99**, 024611 (2019).

[23] J. Bartel, P. Quentin, M. Brack, C. Guet, and H.-B. Hakansson, Nucl. Phys. A **386**, 79 (1982).

[24] J. McDonnell, N. Schunck, and W. Nazarewicz, *Fission and Properties of Neutron-Rich Nuclei* (World Scientific, Singapore, 2013), p. 597.

[25] M. Bender, P. H. Heenen, and P.-G. Reinhard, Rev. Mod. Phys. **75**, 121 (2003).

[26] H. J. Lipkin, Ann. Phys. (NY) **9**, 272 (1960).

[27] Y. Nogami, Phys. Rev. **134**, B313 (1964).

[28] H. C. Pradhan, Y. Nogami, and J. Law, Nucl. Phys. A **201**, 357 (1973).

[29] X. B. Wang, J. Dobaczewski, M. Kortelainen, L. F. Yu, and M. V. Stoitsov, Phys. Rev. C **90**, 014312 (2014).

[30] J. Dobaczewski, W. Nazarewicz, and M. V. Stoitsov, Eur. Phys. J. A **15**, 21 (2002).

[31] R. N. Perez, N. Schunck, R.-D. Lasseri, C. Zhang, and J. Sarich, Comput. Phys. Commun. **220**, 363 (2017).

[32] N. Schunck, Acta Phys. Pol. B **44**, 263 (2013).

[33] W. Younes and D. Gogny, Phys. Rev. C **80**, 054313 (2009).

[34] M. Warda and A. Zdeb, Phys. Scr. **90**, 114003 (2015).

[35] M. Warda, A. Staszczak, and W. Nazarewicz, Phys. Rev. C **86**, 024601 (2012).

[36] J. Sadhukhan, C. L. Zhang, W. Nazarewicz, and N. Schunck, Phys. Rev. C **96**, 061301(R) (2017).

[37] N. Dubray and D. Regnier, Comput. Phys. Commun. **183**, 2035 (2012).

[38] G. F. Bertsch, W. Younes, and L. M. Robledo, Phys. Rev. C **97**, 064619 (2018).

[39] G. F. Bertsch and L. M. Robledo, Phys. Rev. C **100**, 044606 (2019).

[40] P.-G. Reinhard, J. A. Maruhn, A. S. Umar, and V. E. Oberacker, Phys. Rev. C **83**, 034312 (2011).

[41] C. L. Zhang, B. Schuetrumpf, and W. Nazarewicz, Phys. Rev. C **94**, 064323 (2016).

[42] P. Jerabek, B. Schuetrumpf, P. Schwerdtfeger, and W. Nazarewicz, Phys. Rev. Lett. **120**, 053001 (2018).

[43] P. Schillebeeckx, C. Wagemans, A. J. Deruytter, and R. Barthélémy, Nucl. Phys. A **545**, 623 (1992).

[44] K. Nishio, Y. Nakagome, I. Kanno, and I. Kimura, J. Nucl. Sci. Technol. **32**, 404 (1995).

[45] W. Reisdorf, J. P. Unik, H. C. Griffin, and L. E. Glendenin, Nucl. Phys. A **177**, 337 (1971).